Image reconstruction of fluorescent molecular tomography based on the simplified matrix system

Wei Zou,[1,2,3] Jiajun Wang,[1,2,3,*] and David Dagan Feng[2,3,4]

[1]*School of Electronic and Information Engineering, Soochow University, Suzhou 215006, China*
[2]*Department of Electronic and Information Engineering, Hong Kong Polytechnic University, Hong Kong, China*
[3]*School of Information Technologies, The University of Sydney, Sydney, NSW 2006, Australia*
[4]*Med-X Research Institute, Shanghai Jiao Tong University, Shanghai 200030, China*
**Corresponding author: jjwang@suda.edu.cn*

Received February 19, 2013; revised June 6, 2013; accepted June 10, 2013;
posted June 10, 2013 (Doc. ID 185546); published July 3, 2013

Fluorescent molecular tomographic image reconstruction usually involves repeatedly solving large-scale matrix equations, which are computationally expensive. In this paper, a method is proposed to reduce the scale of the matrix system. The Jacobian matrix is simplified by deleting the columns or the rows whose values are smaller than a threshold. Furthermore, the measurement data are divided into two groups and are used for iteration of image reconstruction in turn. The simplified system is then solved in the wavelet domain to further accelerate the process of solving the inverse problem. Simulation results demonstrate that the proposed method can significantly speed up the reconstruction process.

OCIS codes: (100.3190) Inverse problems; (170.3010) Image reconstruction techniques; (170.3880) Medical and biological imaging; (170.6960) Tomography; (260.2510) Fluorescence.
http://dx.doi.org/10.1364/JOSAA.30.001464

1. INTRODUCTION

Optical molecular imaging has been receiving much attention due to its nonionizing, low cost, and high sensitivity. It is widely utilized for drug discovery and tumor detection, as well as intraoperative navigation [1]. Among the optical molecular imaging modalities, fluorescence molecular tomography (FMT) plays an extremely important role because of its abilities to reconstruct the spatial distribution of optical parameters, the fluorescent yield, the fluorescent lifetime, etc. In this imaging modality, a fluorescent biochemical marker used as contrast agent is injected into the biological system and consequently accumulates in diseased tissue as a result of leaky vasculature, hypermetabolism, and angiogenesis [2,3]. During the imaging process, light at the fluorophore's excitation wavelength is used to irradiate the tissue, and then it is absorbed by fluorophore that presents in the tissue. The fluorophore is elevated to an excited state and then decays to the ground state while releasing the energy. This creates fluorescence, which can be separated from the excitation light via interference filters [4]. The fluorescent photon has a longer wavelength than that of the excitation photon, resulting in a color shift. Images of the fluorescent yield and lifetime parameters are reconstructed from several optical measurements on the surface of the tissue [5,6]. At present, FMT has been successfully applied to *in vivo* monitoring inflammation [7], evaluating treatment [8], and investigating breast cancer [9].

Reconstruction of tomographic data involves the generation of a forward model that predicts the observable states as well as an inverse problem to calculate the internal optical and fluorescent properties with the given measured data and sources. One of the major challenges in the reconstruction of FMT is its high computational complexity resulted from extremely large-scale matrix manipulations. In [10], a model-order reduction technique is adopted to reduce the system complexity, where the unknowns are expressed in the subspace with a reduced dimension. However, in this method, a transformation matrix needed to be constructed with the Wilson–Yuan–Dickens basis vectors or the Lanczos basis vectors in the Krylov subspace. Actually, during the process of reconstruction, besides the number of unknowns, the scale of Jacobian matrix and the number of measurement data are two main factors determining the scale of matrix equation and thus determining the speed of the whole process of reconstruction. The manipulation of Jacobian matrix is usually computationally intensive especially for the FMT reconstruction problem, where there are two coupled diffusion equations describing the forward problem. It is well known that the Green's function method is an effective tool for accelerating the Jacobian matrix computing process [11]. However, due to the increasing scale of the matrix, the Green's function method will not work very well. The problem mainly lies in the fact that the Green function method cannot reduce the scale of the Jacobian matrix itself. Therefore, a new method is proposed in this paper to tackle such a problem and accelerate the reconstruction process of FMT. In this method, the Jacobian matrix is simplified by deleting those columns or the rows with values smaller than a predefined threshold. Although the increment of the number of measurement data can improve the quality of reconstruction results, the scale of the matrices involved in the reconstruction of FMT will also become larger, which may slow down the process of tomographic image

reconstruction. To solve that problem, the measurement data are divided into two groups, which are used for iteration of image reconstruction in turn. With this strategy, both the scale of Jacobian matrix and the number of measurement data are reduced during the iteration process of reconstruction. The most important feature of the wavelet transforms lies in the fact that most information of the signal is contained in a small number of entries with other entries being very small and therefore can be neglected [12]. Based on the above simplification in spatial domain, the inverse problem is solved in wavelet domain to improve the efficiency of image reconstruction. Simulation results demonstrate that our proposed algorithm can significantly speed up the reconstruction process at the expense of a small reduction in reconstruction accuracy.

2. FORWARD MODEL

A. Light Transport and Fluorescence Model

Basically, the forward model of FMT can be depicted by two coupled diffusion equations as [13]

$$-\nabla \cdot (D_e \nabla \Phi_e) + k_e \Phi_e = Q_e, \tag{1}$$

$$-\nabla \cdot (D_m \nabla \Phi_m) + k_m \Phi_m = \frac{\phi \mu_{aef}}{1 - i\omega\tau} \Phi_e, \tag{2}$$

where quantities with subscript e and m represent those correspond to the excitation and emission wavelength and $k_{e,m}$ and $D_{e,m}$ can be expressed as

$$k_{e,m} = \mu_{ae,mi} + \mu_{ae,mf} + \frac{i\omega}{c}, \tag{3}$$

$$D_{e,m} = \frac{1}{3(\mu_{ae,mi} + \mu_{ae,mf} + \mu'_{se,m})} \tag{4}$$

with $\mu_{ae,mf}$ and $\mu_{ae,mi}$ being, respectively, the absorption coefficient due to fluorophore and nonfluorescing chromophore, $\mu'_{se,m}$ being the isotropic scattering coefficient, and c representing the speed of light in the medium; $\Phi_{e,m}$ is the photon density, Q_e is the excitation light source, ϕ and τ represent the fluorescence quantum efficiency and fluorescence lifetime.

In our case, the Robin type boundary condition is applied to solve the forward equations.

B. Finite Element Discretization

The forward equations can be solved using the finite element method (FEM). In the framework of FEM, the domain Ω is discretized into P elements connected by N vertex nodes. Upon the discretization procedure [14], Eqs. (1) and (2) can be expressed under the FEM framework as follows:

$$\mathbf{A}_e \Phi_e = \mathbf{Q}_e, \tag{5}$$

$$\mathbf{A}_m \Phi_m = \mathbf{Q}_m. \tag{6}$$

3. RECONSTRUCTION OF FMT

A. Inverse Problem

The task of the inverse problem is to derive the distribution of tissue parameters x with the known distribution of the light sources and the measurements y, i.e.,

$$x = F^{-1}(y), \tag{7}$$

where F is the forward operator.

To linearize the inverse problem, F can be expanded in the vicinity of x_0 in a Taylor series [15]. The Tikhonov regularization term is introduced to improve the ill-posedness of the inverse problem [16]. Therefore, the solution to the inverse problem in a matrix form can be formulated as

$$\Delta \mathbf{x} = (\mathbf{J}^T \mathbf{J} + \lambda \mathbf{I})^{-1} \mathbf{J}^T \Delta \mathbf{y}, \tag{8}$$

where $\Delta \mathbf{x}$ is the perturbation in optical or fluorescent properties, $\Delta \mathbf{y}$ is residual data between the measurements and the predicted data, $\mathbf{J}$ is the Jacobian matrix, $\mathbf{I}$ is the identity matrix, and λ is a regularization parameter.

B. Simplification of the Jacobian Matrix

An $M \times N$ Jacobian matrix can be defined as

$$\mathbf{J} = \begin{bmatrix} \frac{\partial y_1}{\partial x_1} & \cdots & \frac{\partial y_1}{\partial x_N} \\ \vdots & \ddots & \vdots \\ \frac{\partial y_M}{\partial x_1} & \cdots & \frac{\partial y_M}{\partial x_N} \end{bmatrix}. \tag{9}$$

In fact, each element in the Jacobian matrix is just a measure of the rate of change in measurement with respect to the optical parameter [17]. During the iterative process of Eq. (8) for FMT reconstruction, the Jacobian matrix $\mathbf{J}$ needs to be repeatedly updated from iteration to iteration. Therefore, the Jacobian matrix is also a key factor determining the implementation speed of the reconstruction algorithm.

Conventionally, the direct derivation method and the perturbation method are two straightforward methods to obtain the Jacobian matrix. However, the above two methods are computing intensive and are not suitable for obtaining Jacobian matrices with large-scale. Therefore, it is of critical importance to develop an effective Jacobian matrix calculation method for a fast implementation of the reconstruction of FMT. Methods based on the Green's function are typical ones for such a purpose. Although the theory of using the Green's function in the derivation of the Jacobian matrix has been well-established [11], the efficiency of the Green's function method decreases rapidly with the increment of the dimension of the matrix. Therefore, if the scale of the Jacobian matrix can be reduced, the computation efficiency of iterative process will be improved and hence the reconstruction of FMT can also be accelerated.

Each column in the Jacobian matrix corresponds to one node and each element in this column represents the sensitivity of one measurement with respect to that node. When the sum of the absolute values of all the elements in one column is very small (e.g., being smaller than a threshold), it means that the sensitivity for the corresponding node is low. It can be proved [in Appendix A(1)] that the column J_i in the Jacobian matrix can be deleted during the process of

solving Eq. (8) when J_i approaches 0. In such a case, the scale of the Jacobian matrix can be reduced at an expense of little accuracy loss in reconstruction upon deleting those columns. Therefore, the computing efficiency of the iterative process can be improved due to the simplification of the Jacobian matrix. Based on the above idea, an $M \times N$ Jacobian matrix can be simplified by deleting the jth column if the following condition of the parameter SUM is satisfied:

$$\mathrm{SUM} = \sum_{i=1}^{M} |J_{ij}| < a, \tag{10}$$

where a is a threshold and J_{ij} denotes the element of the Jacobian matrix. In this way, the scale of the Jacobian matrix is reduced and hence the process of image reconstruction can be accelerated.

Similarly, it can also be proved [in Appendix A(2)] that the row R_i of the Jacobian matrix can be deleted as R_i approaches 0. Therefore, in order to further improve the reconstruction efficiency, the row of the Jacobian matrix can also be deleted in a similar manner. Suppose that the sum of the absolute values of the ith row of an $M \times N$ Jacobian matrix is smaller than a threshold, i.e.,

$$\sum_{j=1}^{N} |J_{ij}| < a. \tag{11}$$

This inequality implies that sensitivity for the corresponding measurement node is low and hence that row can be deleted. Additionally, since the ith row of the Jacobian matrix relates to the ith component of $\Delta\mathbf{y}$, the deletion of the ith row of the Jacobian matrix implies that the ith element of $\Delta\mathbf{y}$ should also be deleted so that the product of $\mathbf{J}^T\Delta\mathbf{y}$ can be obtained. Therefore, the dimension reduction in the row direction of the Jacobian matrix can lead to the dimension reduction of the residual data $\Delta\mathbf{y}$. In this way, the computational requirement can be significantly reduced.

However, it is possible that there are some prominent elements in the column, where the sum of the absolute values of all the elements in this column is very small. Thus, some useful information will be deleted, which will lead to the poor reconstruction results. To tackle such a problem, another parameter, namely PROPORTION, is introduced in addition to the above mentioned condition in Eq. (10) for determining whether a column in the Jacobian matrix should be deleted. That is, if both of the inequality in Eq. (10) and that in Eq. (12) are satisfied, the column can be deleted:

$$\mathrm{PROPORTION} = \frac{\max_{i=1}^{M} |J_{ij}|}{\sum_{i=1}^{M} |J_{ij}|} < k. \tag{12}$$

In such a way, some useful information may be preserved, especially when the predefined threshold for SUM is large. In our simulations, comparisons will be performed among the results from the algorithm with and without considering the condition in Eq. (12).

In summary, the process for Jacobian matrix simplification can be described in Algorithm 1:

(1) Given x, compute $\Delta\mathbf{y}$ and $\mathbf{J}$ at x;
(2) **for** $(j = 1, \ldots, N)$ **do**
  if $((\sum_{i=1}^{M} |J_{ij}| < a)$ & &$((\max_{i=1}^{M} |J_{ij}| / \sum_{i=1}^{M} |J_{ij}|) < k))$ **then**
   delete the jth column of Jacobian matrix;
   delete the jth element of $\Delta\mathbf{x}$;
  end
 end
(3) **for** $(i = 1, \ldots M$ **do**
  if $(\sum_{j=1}^{N} |J_{ij}| < a)$ **then**
   delete the ith row of Jacobian matrix;
   delete the ith element of $\Delta\mathbf{y}$;
  end
 end

C. Iterative Method Based on the Grouped Measurement Data

Although the increment of the number of measurement data can obviously improve the quality of reconstructed results, the scale of the matrices involved in the reconstruction of FMT will also become larger and larger, which may slow down the process of tomographic image reconstruction. In order to tackle the above problem, we propose to partition the measurement data into two groups that are then used in turn during the iteration process of the reconstruction. That is, one group is used in the first iteration of reconstruction and the other in the next iteration, etc. In this manner, the number of rows in the Jacobian matrix is reduced to one half of that in the Jacobian matrix with all the measurement data involved. Hence both the computational complexity and the computational requirements for the Jacobian matrix are reduced, which will be helpful for reducing the computational burden of our reconstruction problem. One additional superiority of this strategy is that the iterative results from one group of measurement data can provide a good initial guess for the next iteration for the other group of data. Figure 1 gives a schematic illustration of our reconstruction strategy based

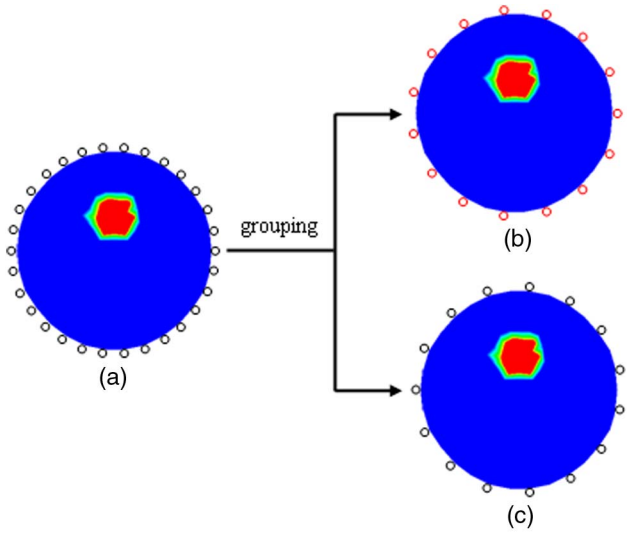

Fig. 1. Scheme of the iteration method based on grouped measurement data: (a) measurement data without grouping, (b) measurement data of red group, and (c) measurement data of black group.

on two groups of measurement data used in turn in the iterations of the reconstruction. Figure 1(a) illustrates the measurement data without being grouped. In Figs. 1(b) and 1(c), the two groups of measurement data are illustrated with black circles and red circles, respectively.

D. Image Reconstruction Based on the Wavelet Transform

It is well known that the most important feature of the wavelet transforms lies in the fact that most information of the signal is contained in a small number of entries with other entries being very small and therefore can be neglected [12]. Some related research on wavelet-based image reconstruction has been conducted. In [18], a time-resolved forward model and its projection onto wavelet basis functions have been implemented. Ducros *et al.* apply compression techniques to the measurements acquired with structured illuminations [19]. That method is based on the exploitation of the wavelet transform of the measurements acquired after wavelet-patterned illuminations. In [20], a multiresolution technique that uses wavelet decomposition is chosen to reduce computation complexity in the modeling stage. All the matrices are projected onto an orthonormal wavelet basis and reduced according to the wavelet's properties.

To exploit the multiresolution property of the wavelet and further reduce the time of reconstruction process, the simplified system is solved in the wavelet domain upon performing wavelet transform in this paper. For such a purpose, Eq. (8) can be rewritten as

$$\mathbf{K}\Delta\mathbf{x} = \mathbf{b} \tag{13}$$

with $\mathbf{K} = (\mathbf{J}^T\mathbf{J} + \lambda\mathbf{I})$ and $\mathbf{b} = \mathbf{J}^T\Delta\mathbf{y}$.

In Eq. (13), upon connecting all the rows in a head to tail manner, the perturbations of the two-dimensional optical parameters is represented with a one-dimensional vector $\Delta\mathbf{x}$. To solve the simplified system in the wavelet domain, we perform the wavelet transform in both sides of Eq. (13) and have

$$\hat{\mathbf{K}}\Delta\hat{\mathbf{x}} = \hat{\mathbf{b}}, \tag{14}$$

where $\hat{\mathbf{K}} = \mathbf{W_b}\mathbf{K}\mathbf{W}_\mathbf{x}^T$, $\Delta\hat{\mathbf{x}} = \mathbf{W_x}\Delta\mathbf{x}$, $\hat{\mathbf{b}} = \mathbf{W_b}\mathbf{b}$, $\mathbf{W_x}$, and $\mathbf{W_b}$ are, respectively, the wavelet transform matrix of $\Delta\mathbf{x}$ and $\mathbf{b}$; $\mathbf{W_x}$ is an orthonormal matrix.

From Eq. (14), it can be seen that the wavelet transform conducted in Eq. (13) leads to the multiresolution representation of the original signals, such as one-dimensional discrete signal $\Delta\mathbf{x}$ and $\mathbf{b}$ as well as two-dimensional signal $\mathbf{K}$. Basically, the signal $\Delta\mathbf{x}$ and $\mathbf{b}$ with N components can be described as

$$\Delta\hat{\mathbf{x}}_{N\times 1} = \begin{bmatrix} A_{-1}\Delta\mathbf{x}_{N/2\times 1} \\ D_{-1}\Delta\mathbf{x}_{N/2\times 1} \end{bmatrix}, \qquad \hat{\mathbf{b}}_{N\times 1} = \begin{bmatrix} A_{-1}\mathbf{b}_{N/2\times 1} \\ D_{-1}\mathbf{b}_{N/2\times 1} \end{bmatrix}. \tag{15}$$

It can be seen from this equation that the original signal can be decomposed into two parts of the approximation component as $A_{-1}\Delta\mathbf{x}_{N/2\times 1}$ or $A_{-1}\mathbf{b}_{N/2\times 1}$ and the detail component as $D_{-1}\Delta\mathbf{x}_{N/2\times 1}$ or $D_{-1}\mathbf{b}_{N/2\times 1}$.

Similarly, the two-level wavelet-based multiresolution representation of $\mathbf{K}$ sized $N\times N$ can be expressed with the following formula:

$$\hat{\mathbf{K}}_{N\times N} = \begin{bmatrix} A_{-1}\mathbf{K}_{N/2\times N/2} & D^1_{-1}\mathbf{K}_{N/2\times N/2} \\ D^2_{-1}\mathbf{K}_{N/2\times N/2} & D^3_{-1}\mathbf{K}_{N/2\times N/2} \end{bmatrix}. \tag{16}$$

Four elements in the matrix of the right-hand side of Eq. (16) are, respectively, the approximation image $A_{-1}\mathbf{K}_{N/2\times N/2}$ and three detail images $D^1_{-1}\mathbf{K}_{N/2\times N/2}$, $D^2_{-1}\mathbf{K}_{N/2\times N/2}$ and $D^3_{-1}\mathbf{K}_{N/2\times N/2}$.

The wavelet transform can be successively performed level by level with respect to the approximation components in both sides of Eq. (14) to obtain a multiresolution representation of the reconstruction problem.

E. Algorithm Description

Actually, the solution to the reconstruction problem can be obtained by minimizing the residue between the measured and predicted data as follows:

$$\psi(\mathbf{x}) = \frac{1}{2}(\mathbf{y} - F(\mathbf{x}))^T(\mathbf{y} - F(\mathbf{x})), \tag{17}$$

where $\psi(\mathbf{x})$ is the objective function measuring the discrepancy between the measured and predicted data. $\mathbf{y}$ is a vector of the measured data on the boundary, and $F(\mathbf{x})$ is a vector of the predicted data on the boundary according to a forward model. Therefore, the reconstruction problem can be regarded as an optimization problem minimizing $\psi(\mathbf{x})$ with respect to $\mathbf{x}$. In terms of this, the whole reconstruction algorithm can be summarized in Algorithm 2:

(1) Set $\mathbf{x}_0$ to an initial guess, $\mathbf{x} = \mathbf{x}_0$; Set $i = 2$;
(2) **if** (i%2==0) **then**
  Compute $\Delta\mathbf{y}$ and $\mathbf{J}$ at x with Algorithm 1 based on the first group of measurement data;
  else
  Compute $\Delta\mathbf{y}$ and $\mathbf{J}$ at x with Algorithm 1 based on the second group of measurement data;
  end
  $i = i + 1$;
(3) **for** ($l = -1, \ldots, -L$) **do**
  Perform wavelet transform for $\mathbf{K}$ and $\mathbf{b}$ to obtain $\hat{\mathbf{K}}_l$ and $\hat{\mathbf{b}}_l$, which are the wavelet transform at the lth level for $\mathbf{K}$ and $\mathbf{b}$, respectively;
  end
  Set $l = -L$ and $\Delta\hat{\mathbf{x}}^{(0)}_{-L} = 0$;
(4) **while** ($l < 0$) **do**
  Obtain a solution from $\hat{\mathbf{K}}_l\Delta\hat{\mathbf{x}}_l = \hat{\mathbf{b}}_l$ using the CGD method with an initial value $\Delta\hat{\mathbf{x}}^{(0)}_l$;
  Prolongate $\Delta\hat{\mathbf{x}}_l$ through padding zeros to obtain an initial guess for $\Delta\hat{\mathbf{x}}_{l+1}$ at the next higher resolution, i.e., $\Delta\hat{\mathbf{x}}^{(0)}_{l+1} = [\Delta\hat{\mathbf{x}}^T_l, \mathbf{0}^T]^T$;
  $l = l + 1$;
  end
  Solve $\mathbf{K}\Delta\mathbf{x} = \mathbf{b}$ with $\Delta\mathbf{x}^{(0)} = \mathbf{W}_\mathbf{x}^T\Delta\hat{\mathbf{x}}^{(0)}_0$ as an initial guess;
  Update $\mathbf{x}$ using Eq. (13) and compute the corresponding objective function $\psi(\mathbf{x})$ according to Eq. (17);
(5) **if** ($\psi(\mathbf{x}) < \delta$) **then**
  Stop and output $\mathbf{x}$;
  else
  Go to step (2);
  end

Based on the proposed algorithms, the matrix system of reconstruction is simplified in both of the spatial domain and wavelet domain, which can improve the efficiency of reconstruction.

4. SIMULATION RESULTS AND DISCUSSION

To evaluate the performance of our proposed algorithm, simulation experiments are implemented. The simulated forward data are obtained from the diffusion equations as illustrated in Eqs. (1) and (2), where Gaussian noise with a signal-to-noise ratio of 10 dB is added for evaluating the noise robustness of the algorithms. Figure 2 illustrates the simulated phantoms with one anomaly in Fig. 2(a) and two anomalies of different shapes in Fig. 2(b). Four sources and 30 detectors are equally distributed around the circumference of the simulated phantom.

The accuracy of FEM solutions to the partial differential equations depends on the mesh size. To reduce the computation requirements without significantly reducing the image resolution, the image reconstruction is implemented based on an adaptively refined mesh. During the process of

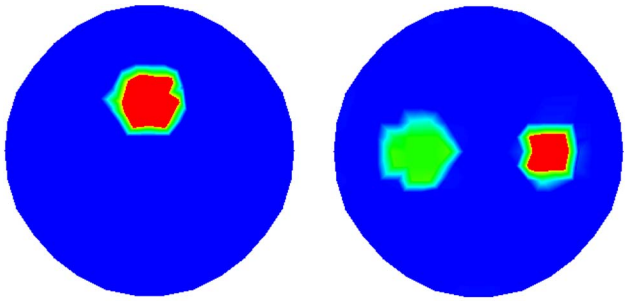

Fig. 2. Simulated phantoms for reconstruction of FMT (a) with one anomaly and (b) with two anomalies.

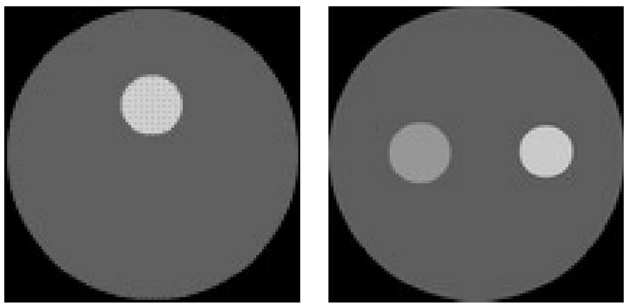

Fig. 3. Prior images used for (a) one-anomaly phantom and (b) two-anomaly phantom.

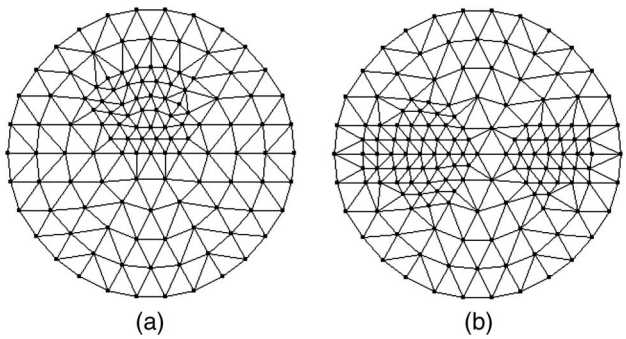

Fig. 4. Adaptively refined meshes for reconstruction of FMT for (a) one-anomaly phantom and (b) two-anomaly phantom.

Table 1. Optical and Fluorescent Properties of One-Anomaly Phantom

Excitation Light	μ_{aef} (mm^{-1})	μ_{aei} (mm^{-1})	μ'_{se} (mm^{-1})	ϕ	τ (ns)
Anomaly	0.3	0.03	4.0	0.2	0.6
Background	0.05	0.03	4.0	0.2	0.6
Fluorescent light	μ_{amf} (mm^{-1})	μ_{ami} (mm^{-1})	μ'_{sm} (mm^{-1})	ϕ	τ (ns)
Anomaly	0.2	0.02	3.0	0.2	0.6
Background	0.005	0.02	3.0	0.2	0.6

Table 2. Optical and Fluorescent Properties of Two-Anomaly Phantom

Excitation Light	μ_{aef} (mm^{-1})	μ_{aei} (mm^{-1})	μ'_{se} (mm^{-1})	ϕ	τ (ns)
Anomalies	0.2, 0.3	0.03	4.0	0.2	0.6
Background	0.05	0.03	4.0	0.2	0.6
Fluorescent light	μ_{amf} (mm^{-1})	μ_{ami} (mm^{-1})	μ'_{sm} (mm^{-1})	ϕ	τ (ns)
Anomalies	0.02, 0.03	0.02	3.0	0.2	0.6
Background	0.003	0.02	3.0	0.2	0.6

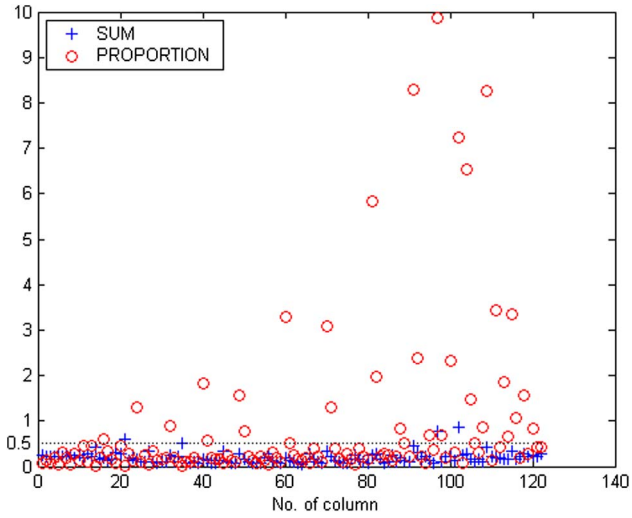

Fig. 5. Distributions of SUMs and PROPORTIONs.

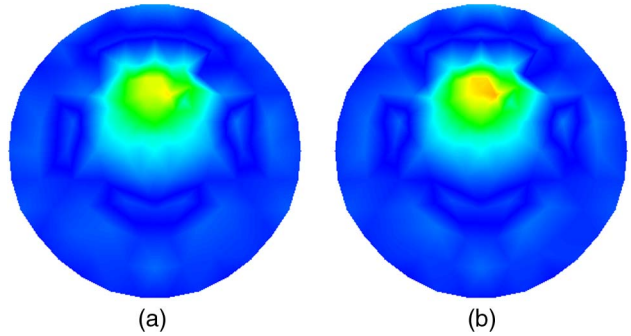

Fig. 6. Reconstructed results of absorption coefficient μ_{aef} (a) without the condition for PROPORTION and (b) with the condition for PROPORTION.

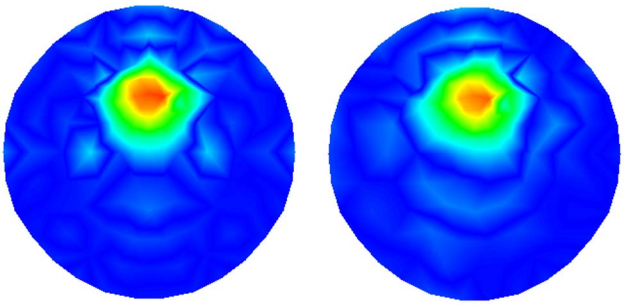

Fig. 7. Reconstructed results of absorption coefficient μ_{aef} for phantom with one anomaly based on (a) method without simplified matrix system and (b) proposed method.

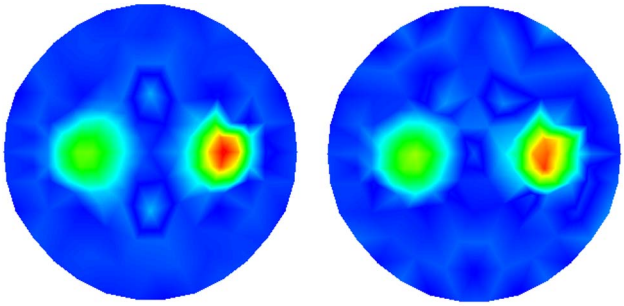

Fig. 8. Reconstructed results of absorption coefficient μ_{aef} for phantom with two anomalies based on (a) method without simplified matrix system and (b) proposed method.

Table 3. Performance Comparison of Reconstruction Methods for Phantom with One Anomaly

Methods	Our Algorithm	Method without Simplified Matrix System
Computation time (s)	152	218
MSE	4.803×10^{-4}	4.792×10^{-4}

Table 4. Performance Comparison of Reconstruction Methods for Phantom with Two Anomalies

Methods	Our Algorithm	Method without Simplified Matrix System
Computation time (s)	211	290
MSE	2.845×10^{-4}	2.814×10^{-4}

Table 5. Performance Comparison of Reconstruction Methods for Three Techniques

Methods	Method in Fig. 9(a)	Method in Fig. 9(b)	Method in Fig. 9(c)
Computation time (s)	241	235	211
MSE	2.986×10^{-4}	2.981×10^{-4}	2.845×10^{-4}

mesh generation, some *a priori* information derived from other imaging modalities, such as the structural imaging can be incorporated. The reconstructed domain is first uniformly discretized according to the Delaunay triangulation scheme, after which the uniform mesh is then adaptively refined in combination with the *a priori* information. The areas with fine details should be reconstructed with high resolution, whereas other areas composed mainly of the low-frequency component with little variation can be reconstructed with low resolution to reduce the computational requirements and also to improve the ill-posedness. Based on this idea, the a priori images with a resolution of 100×100 pixels, as shown in Figs. 3(a) and 3(b) corresponding to Figs. 2(a) and 2(b), respectively, are used to generate the adaptively refined meshes. In Fig. 4, (a) shows the adaptively refined mesh with 122 nodes and 212 triangular elements, while (b) gives the one with 148 nodes and 264 triangular elements, both of which are generated with the prior information, as shown in Figs. 3(a) and 3(b) incorporated, respectively.

Tables 1 and 2 outline the optical and fluorescent parameters in different areas of the simulated phantoms corresponding to Figs. 2(a) and 2(b), respectively. To quantitatively assess the accuracy of the different algorithms, the mean square error (MSE) is introduced as a measure:

$$\mathrm{MSE} = \sum_{i=1}^{N} \left\{ \frac{1}{N} (x^{\mathrm{cal}} - x^{\mathrm{act}})_i^2 \right\}, \tag{18}$$

where N is the total number of nodes in the domain. The superscript cal denotes the values obtained using reconstruction algorithms and act denotes the actual distribution of the optical or fluorescent parameters, which are used to generate the synthetic image data set.

In this work, assuming that the scattering coefficients are known, we focus on the reconstruction of the absorption coefficient μ_{aef}. As Daubechies 1 (Haar wavelet) has advantages, such as orthogonality and symmetry, the Daubechies 1 wavelet is used in the simulations [21]. For a convenience of the

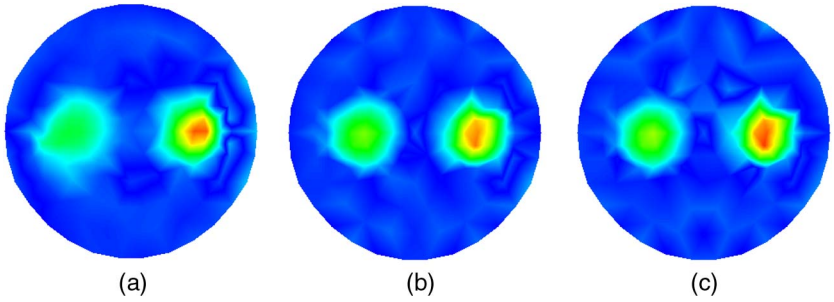

Fig. 9. Reconstructed results of absorption coefficient μ_{aef} based on (a) simplification of the Jacobian matrix, (b) combined simplification of the Jacobian matrix and grouped measurement data, and (c) proposed algorithm.

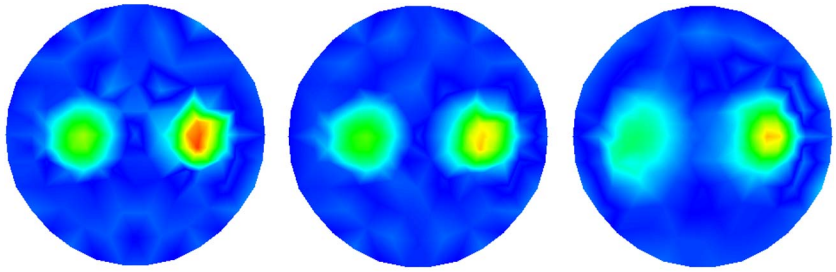

Fig. 10. Reconstructed results of absorption coefficient μ_{aef} for phantom of two anomalies with the value of c being (a) 0.05, (b) 0.1, and (c) 0.2, respectively.

following discussion, the threshold a is selected so that the following equation is satisfied:

$$a = c \times \sum_{i=1}^{M} \sum_{j=1}^{N} |J_{ij}|, \tag{19}$$

where J_{ij} denotes the element of an $M \times N$ Jacobian matrix.

To determine a proper threshold for PROPORTION, we analyze the distribution of the elements in the columns of Jacobian matrix for one-anomaly phantom with one source. Based on this distribution, the distributions of SUMs and PROPORTIONs can be calculated whose results are shown in Fig. 5. It can be seen from this figure that most of PROPORTION are less than 50%, which can be set as the value of k in step (2) of Algorithm 1. Figure 6 shows the reconstructed results of μ_{aef} with $c = 0.2$. It can be seen that the reconstruction quality can be improved especially for the area of anomaly if the condition of PROPORTION is considered. Therefore, all the subsequent simulation results in this paper are from our proposed algorithm with the condition of PROPORTION considered.

Table 6. Impact of the Threshold on the Reconstruction for Phantom with Two Anomalies

c	0.05	0.1	0.2
Computation time (s)	211	185	160
MSE	2.845×10^{-4}	3.982×10^{-4}	6.015×10^{-3}

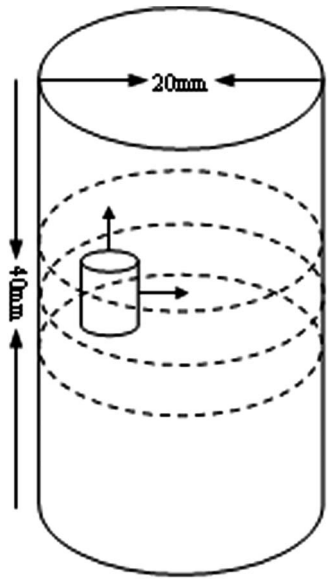

Fig. 11. Simulated phantom for 3D reconstruction. The phantom of radius 10 mm and height 40 mm with a uniform background of $\mu_{aef} = 0.005$ mm^{-1}, which is positioned at $x = 10$ mm, $y = 0$ mm, and $z = 20$ mm. The small cylindrical anomaly has a radius of 2 mm and height 6 mm with $\mu_{aef} = 0.01$ mm^{-1}.The anomaly is positioned at $x = 5$ mm, $y = 0$ mm, and $z = 20$ mm. The dashed curves represent the measurement planes, at $z = 15$ mm, $z = 20$ mm, $z = 25$ mm.

The reconstructed images of μ_{aef} for the phantom with one anomaly using different algorithms are shown in Fig. 7, where Fig. 7(a) shows the reconstructed result from the method without using the simplified matrix system, and Fig. 7(b) depicts the reconstructed result from the proposed method with c being selected as 0.05. The reconstructed images of μ_{aef} for phantom with two anomalies using different algorithms are illustrated in Fig. 8. The reconstruction result from the method without using the simplified matrix system and the reconstruction result from our method with $c = 0.05$ are shown in Figs. 8(a) and 8(b), respectively.

To further evaluate the reconstruction quality, Tables 3 and 4 summarize the performance of reconstructions in terms of the computation time and MSE as defined in Eq. (18) for phantoms with one anomaly and two anomalies, respectively. From these tables, it can be seen that our proposed algorithm can significantly speed up the reconstruction process at the expense of a small reduction in reconstruction accuracy.

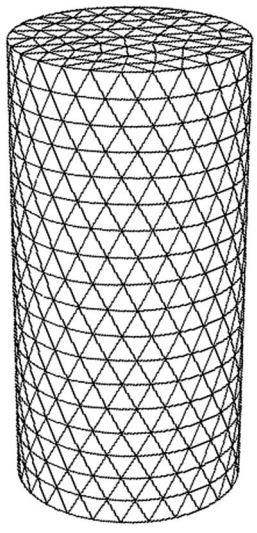

Fig. 12. 3D mesh for image reconstruction.

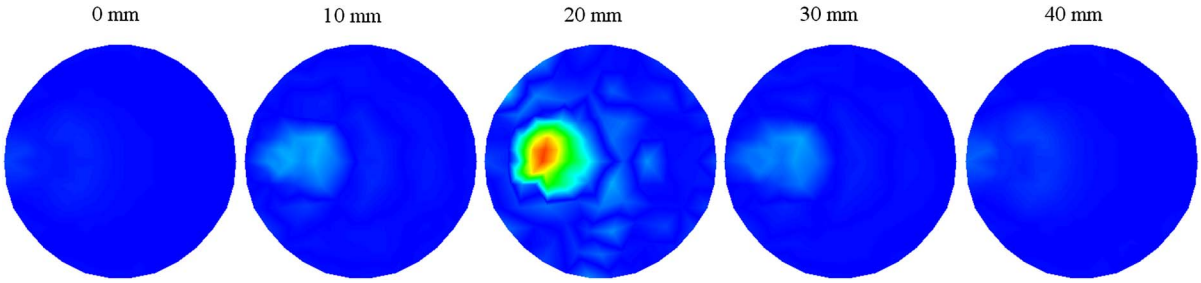

Fig. 13. Reconstructed images using the proposed algorithm, which are 2D cross sections through the reconstructed 3D volume. The right-hand side corresponds to the top of the cylinder ($z = 40$ mm) and the left corresponds to the bottom of the cylinder ($z = 0$ mm), with each slice representing a 10 mm increment.

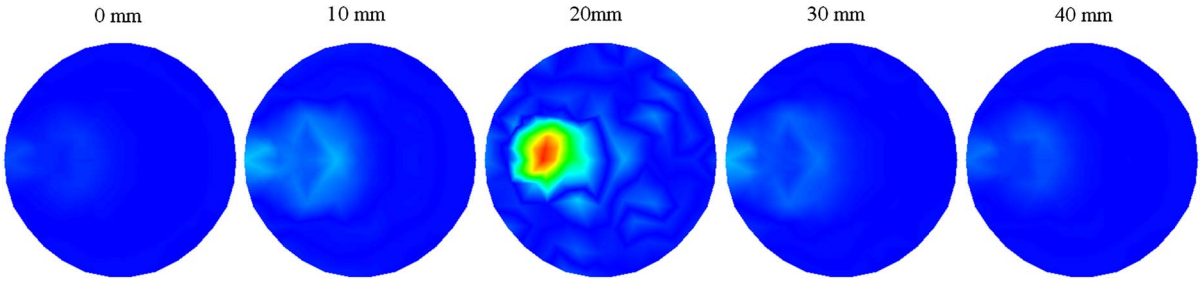

Fig. 14. Reconstructed images using the method without simplified matrix system, which are 2D cross sections through the reconstructed 3D volume. The right-hand side corresponds to the top of the cylinder ($z = 40$ mm), and the left corresponds to the bottom of the cylinder ($z = 0$ mm), with each slice representing a 10 mm increment.

Actually, three techniques are included in the proposed algorithm as described in Subsections 3.B, 3.C, and 3.D. To illustrate the contribution to the performance from each of these three techniques, Fig. 9 gives the reconstructed results for phantom with two anomalies under different combination of the above mentioned techniques. Quantitative comparisons of the reconstructed results are listed in Table 5. From this table, it can be seen that, in this simulated reconstruction, the method of simplification of the Jacobian matrix contributes most to about 62% of the reconstruction acceleration. The wavelet method and strategy of grouped measurement data contribute to about 30% and 8% of the reconstruction acceleration, respectively. Furthermore, the simplification of the Jacobian matrix may increase MSE while the wavelet method can improve the quality of reconstruction by decreasing about 5% of MSE.

To investigate the impact of the threshold on the MSE and the computation time, the reconstructions are implemented using our proposed algorithm with different settings of c. The reconstructed results under different settings of c for phantom with two anomalies are shown in Figs. 10(a)–10(c) with c being set as 0.05, 0.1, and 0.2, respectively. Table 6 lists the corresponding performance of reconstruction under different settings of the threshold (i.e., c). It can be seen that, when the threshold becomes larger, the reconstruction speed can be further improved, but it results in a relatively larger MSE. A similar conclusion can also be drawn for the case of one anomaly. This means that our algorithm can significantly speed up the process of reconstruction at the expense of a small reduction in reconstruction accuracy.

To further validate the proposed algorithm for 3D reconstruction, we extend the methods previously defined for triangular elements to tetrahedral elements. The integration of products of shape functions over the volume of the elements, and surface integrals over a side of the element, as required for the computation of element stiffness and mass matrices, is performed by a numerical integration rules.

In the 3D case, a cylindrical phantom as illustrated schematically in Fig. 11 is used for simulations. Within this phantom, a small cylindrical object is suspended. The dashed curves represent the planes of measurement. Four sources and 16 measurements are used for each plane in the simulations. The data are collected in all three measurement planes. The mesh for reconstructing the 3D image as shown in Fig. 12 contains 858 nodes and 3208 tetrahedral elements. Figures 13 and 14 depict the 3D reconstructed images using the proposed algorithm and the method without using the simplified matrix system, respectively. These are 2D cross sections through the reconstructed 3D images. Table 7 lists the performance of the above two methods for a quantitative comparison. From this table, we can conclude that our proposed algorithm can also

Table 7. Performance Comparison of 3D Reconstruction Methods

Methods	Our Algorithm	Method without Simplified Matrix System
Computation time (s)	2541	3748
MSE	3.992×10^{-3}	3.869×10^{-3}

significantly speed up the reconstruction process for the 3D case.

5. CONCLUSION

In this paper, a new method based on a simplified matrix system is proposed for image reconstruction of FMT. In this method, the traditional computationally intensive Jacobian matrix is simplified by deleting the rows or columns whose values are smaller than the threshold. In order to further reduce the scale of Jacobian matrix as well as the number of measurement data involved in each iteration, the measurement data are divided into two groups that are used in turn in the iterations of reconstruction. The simplified system is solved in wavelet domain to further accelerate process of solving the inverse problem. Simulation results show that our algorithm can significantly accelerate the reconstruction process.

APPENDIX A

(1) Proof. □

Let

$$\Delta\mathbf{x} = (\,\Delta x_1 \quad \Delta x_2 \quad \cdots \quad \Delta x_i \quad \cdots \quad \Delta x_N\,)^T \qquad (\Delta\mathbf{x} \in \mathbb{R}^N)$$

and

$$\mathbf{J} = (\,J_1 \quad J_2 \quad \cdots \quad J_i \quad \cdots \quad J_N\,) \qquad (\mathbf{J} \in \mathbb{R}^{M\times N})$$

denote a vector of the perturbation in optical parameters and the Jacobian matrix, respectively. Substituting them into Eq. (8), we have

$$\left[\begin{pmatrix} J_1^T \\ J_2^T \\ \vdots \\ J_i^T \\ \vdots \\ J_N^T \end{pmatrix} \cdot (J_1 \quad J_2 \quad \cdots \quad J_i \quad \cdots \quad J_N) + \lambda\mathbf{I}\right] \cdot \begin{pmatrix} \Delta x_1 \\ \Delta x_2 \\ \vdots \\ \Delta x_i \\ \vdots \\ \Delta x_N \end{pmatrix} = \begin{pmatrix} J_1^T \\ J_2^T \\ \vdots \\ J_i^T \\ \vdots \\ J_N^T \end{pmatrix} \cdot \Delta\mathbf{y}. \tag{A1}$$

Equation (A1) can be further written as

$$\begin{pmatrix} J_1^TJ_1+\lambda & J_1^TJ_2 & \cdots & J_1^TJ_i & \cdots & J_1^TJ_N \\ J_2^TJ_1 & J_2^TJ_2+\lambda & \cdots & J_2^TJ_i & \cdots & J_2^TJ_N \\ \vdots & \vdots & \ddots & \vdots & & \vdots \\ J_i^TJ_1 & J_i^TJ_2 & \cdots & J_i^TJ_i+\lambda & \cdots & J_i^TJ_N \\ \vdots & \vdots & & \vdots & \ddots & \vdots \\ J_N^TJ_1 & J_N^TJ_2 & \cdots & J_N^TJ_i & \cdots & J_N^TJ_N+\lambda \end{pmatrix} \cdot \begin{pmatrix} \Delta x_1 \\ \Delta x_2 \\ \vdots \\ \Delta x_i \\ \vdots \\ \Delta x_N \end{pmatrix} = \begin{pmatrix} J_1^T\cdot\Delta\mathbf{y} \\ J_2^T\cdot\Delta\mathbf{y} \\ \vdots \\ J_i^T\cdot\Delta\mathbf{y} \\ \vdots \\ J_N^T\cdot\Delta\mathbf{y} \end{pmatrix}, \tag{A2}$$

From Eq. (A2), it can be seen that the above matrix equation is composed of N equations, and the ith equation can be expressed as

$$(J_i^TJ_1 \quad J_i^TJ_2 \quad \cdots \quad J_i^TJ_i+\lambda \quad \cdots \quad J_i^TJ_N)\cdot\Delta\mathbf{x} = J_i^T\cdot\Delta\mathbf{y}. \tag{A3}$$

Then, we have

$$\Delta x_i = \frac{J_i^T(\Delta\mathbf{y}-\Delta x_1J_1-\Delta x_2J_2\cdots-\Delta x_{i-1}J_{i-1}-\Delta x_{i+1}J_{i+1}\cdots-\Delta x_NJ_N)}{J_i^TJ_i+\lambda}. \tag{A4}$$

The limit of Δx_i as J_i approaches 0 can be achieved as

$$\lim_{J_i\to 0}\Delta x_i = \lim_{J_i\to 0}\frac{J_i^T(\Delta\mathbf{y}-\Delta x_1J_1-\Delta x_2J_2\cdots-\Delta x_{i-1}J_{i-1}-\Delta x_{i+1}J_{i+1}\cdots-\Delta x_NJ_N)}{J_i^TJ_i+\lambda} = 0. \tag{A5}$$

For convenience of the following discussion, Eq. (A1) can be rewritten as

$$\begin{pmatrix} J_1^T\mathbf{J}\Delta\mathbf{x} \\ J_2^T\mathbf{J}\Delta\mathbf{x} \\ \vdots \\ J_i^T\mathbf{J}\Delta\mathbf{x} \\ \vdots \\ J_N^T\mathbf{J}\Delta\mathbf{x} \end{pmatrix} + \lambda\mathbf{I}\cdot\begin{pmatrix} \Delta x_1 \\ \Delta x_2 \\ \vdots \\ \Delta x_i \\ \vdots \\ \Delta x_N \end{pmatrix} = \begin{pmatrix} J_1^T\Delta\mathbf{y} \\ J_2^T\Delta\mathbf{y} \\ \vdots \\ J_i^T\Delta\mathbf{y} \\ \vdots \\ J_N^T\Delta\mathbf{y} \end{pmatrix}. \tag{A6}$$

For the case when J_i approaches 0, we have

$$\lim_{J_i\to 0}\left[\begin{pmatrix} J_1^T\mathbf{J}\Delta\mathbf{x} \\ J_2^T\mathbf{J}\Delta\mathbf{x} \\ \vdots \\ J_i^T\mathbf{J}\Delta\mathbf{x} \\ \vdots \\ J_N^T\mathbf{J}\Delta\mathbf{x} \end{pmatrix} + \lambda\mathbf{I}\cdot\begin{pmatrix} \Delta x_1 \\ \Delta x_2 \\ \vdots \\ \Delta x_i \\ \vdots \\ \Delta x_N \end{pmatrix}\right] = \lim_{J_i\to 0}\begin{pmatrix} J_1^T\Delta\mathbf{y} \\ J_2^T\Delta\mathbf{y} \\ \vdots \\ J_i^T\Delta\mathbf{y} \\ \vdots \\ J_N^T\Delta\mathbf{y} \end{pmatrix}. \tag{A7}$$

Since $\lim_{J_i\to 0} J_i^T\mathbf{J}\Delta\mathbf{x} = 0$, $\lim_{J_i\to 0}\Delta x_i = 0$ and $\lim_{J_i\to 0} J_i^T\Delta\mathbf{y} = 0$, we have

$$\lim_{J_i\to 0}\left[\begin{pmatrix} J_1^T\mathbf{J}\Delta\mathbf{x} \\ J_2^T\mathbf{J}\Delta\mathbf{x} \\ \vdots \\ J_{i-1}^T\mathbf{J}\Delta\mathbf{x} \\ 0 \\ J_{i+1}^T\mathbf{J}\Delta\mathbf{x} \\ \vdots \\ J_N^T\mathbf{J}\Delta\mathbf{x} \end{pmatrix} + \lambda\mathbf{I}\cdot\begin{pmatrix} \Delta x_1 \\ \Delta x_2 \\ \vdots \\ \Delta x_{i-1} \\ 0 \\ \Delta x_{i+1} \\ \vdots \\ \Delta x_N \end{pmatrix}\right] = \lim_{J_i\to 0}\begin{pmatrix} J_1^T\Delta\mathbf{y} \\ J_2^T\Delta\mathbf{y} \\ \vdots \\ J_{i-1}^T\Delta\mathbf{y} \\ 0 \\ J_{i+1}^T\Delta\mathbf{y} \\ \vdots \\ J_N^T\Delta\mathbf{y} \end{pmatrix}. \tag{A8}$$

From Eq. (A8), we can obtain

$$\lim_{J_i\to 0}\left[\begin{pmatrix} J_1^T\mathbf{J}\Delta\mathbf{x} \\ J_2^T\mathbf{J}\Delta\mathbf{x} \\ \vdots \\ J_{i-1}^T\mathbf{J}\Delta\mathbf{x} \\ J_{i+1}^T\mathbf{J}\Delta\mathbf{x} \\ \vdots \\ J_N^T\mathbf{J}\Delta\mathbf{x} \end{pmatrix} + \lambda\mathbf{I}\cdot\begin{pmatrix} \Delta x_1 \\ \Delta x_2 \\ \vdots \\ \Delta x_{i-1} \\ \Delta x_{i+1} \\ \vdots \\ \Delta x_N \end{pmatrix}\right] = \lim_{J_i\to 0}\begin{pmatrix} J_1^T\Delta\mathbf{y} \\ J_2^T\Delta\mathbf{y} \\ \vdots \\ J_{i-1}^T\Delta\mathbf{y} \\ J_{i+1}^T\Delta\mathbf{y} \\ \vdots \\ J_N^T\Delta\mathbf{y} \end{pmatrix}. \tag{A9}$$

The above equation can be further written as

$$\lim_{J_i\to 0}\begin{pmatrix} J_1^T \\ J_2^T \\ \vdots \\ J_{i-1}^T \\ J_{i+1}^T \\ \vdots \\ J_N^T \end{pmatrix}\cdot(J_1\Delta x_1 + J_2\Delta x_2 + \cdots + J_i\Delta x_i + \cdots J_N\Delta x_N)$$

$$+\lambda\mathbf{I}\cdot\begin{pmatrix} \Delta x_1 \\ \Delta x_2 \\ \vdots \\ \Delta x_{i-1} \\ \Delta x_{i+1} \\ \vdots \\ \Delta x_N \end{pmatrix}\Bigg] = \lim_{J_i\to 0}\begin{pmatrix} J_1^T\Delta\mathbf{y} \\ J_2^T\Delta\mathbf{y} \\ \vdots \\ J_{i-1}^T\Delta\mathbf{y} \\ J_{i+1}^T\Delta\mathbf{y} \\ \vdots \\ J_N^T\Delta\mathbf{y} \end{pmatrix}. \tag{A10}$$

Since $\lim_{J_i\to 0} J_i\Delta x_i = 0$, we have

$$\lim_{J_i\to 0}\left[\begin{pmatrix} J_1^T \\ J_2^T \\ \vdots \\ J_{i-1}^T \\ J_{i+1}^T \\ \vdots \\ J_N^T \end{pmatrix}(J_1\Delta x_1 + J_2\Delta x_2 + \cdots + J_{i-1}\Delta x_{i-1}\right.$$

$$\left.+J_{i+1}\Delta x_{i+1}\cdots J_N\Delta x_N) + \lambda\mathbf{I}\cdot\begin{pmatrix} \Delta x_1 \\ \Delta x_2 \\ \vdots \\ \Delta x_{i-1} \\ \Delta x_{i+1} \\ \vdots \\ \Delta x_N \end{pmatrix}\right]$$

$$= \lim_{J_i\to 0}\begin{pmatrix} J_1^T\Delta\mathbf{y} \\ J_2^T\Delta\mathbf{y} \\ \vdots \\ J_{i-1}^T\Delta\mathbf{y} \\ J_{i+1}^T\Delta\mathbf{y} \\ \vdots \\ J_N^T\Delta\mathbf{y} \end{pmatrix}. \tag{A11}$$

Then, we can further obtain

$$\lim_{J_i\to 0}\left[\begin{pmatrix} J_1^T \\ J_2^T \\ \vdots \\ J_{i-1}^T \\ J_{i+1}^T \\ \vdots \\ J_N^T \end{pmatrix}\cdot(J_1 \quad J_2 \quad \cdots \quad J_{i-1} \quad J_{i+1} \quad \cdots \quad J_N) + \lambda\mathbf{I}\right]$$

$$\cdot\begin{pmatrix} \Delta x_1 \\ \Delta x_2 \\ \vdots \\ \Delta x_{i-1} \\ \Delta x_{i+1} \\ \vdots \\ \Delta x_N \end{pmatrix} = \lim_{J_i\to 0}\begin{pmatrix} J_1^T \\ J_2^T \\ \vdots \\ J_{i-1}^T \\ J_{i+1}^T \\ \vdots \\ J_N^T \end{pmatrix}\cdot\Delta\mathbf{y}. \tag{A12}$$

From Eqs. (A1) and (A12), it can be seen that the ith column J_i of the Jacobian matrix can be deleted as J_i approaches 0 during solving Eq. (8).

(2) Proof. □
Let

$$\Delta\mathbf{y} = (\,\Delta y_1 \quad \Delta y_2 \quad \cdots \quad \Delta y_i \quad \cdots \quad \Delta y_M\,)^T \qquad (\Delta\mathbf{y} \in \mathbb{R}^M)$$

and

$$\mathbf{J} = (\,R_1^T \quad R_2^T \quad \cdots \quad R_i^T \quad \cdots \quad R_M^T\,)^T \qquad (\mathbf{J} \in \mathbb{R}^{M\times N})$$

denote the vector for residual data between the measurements and the predicted data, and the Jacobian matrix, respectively. Substituting them into Eq. (8), we have

$$\left[(R_1^T \quad R_2^T \quad \cdots \quad R_i^T \quad \cdots \quad R_M^T)\cdot\begin{pmatrix} R_1 \\ R_2 \\ \vdots \\ R_i \\ \vdots \\ R_M \end{pmatrix} + \lambda\mathbf{I}\right]\cdot\Delta\mathbf{x}$$

$$= (R_1^T \quad R_2^T \quad \cdots \quad R_i^T \quad \cdots \quad R_M^T)\cdot\begin{pmatrix} \Delta y_1 \\ \Delta y_2 \\ \vdots \\ \Delta y_i \\ \vdots \\ \Delta y_M \end{pmatrix}. \tag{A13}$$

From the above equation, we have

$$[(R_1^TR_1 + R_2^TR_2 + \cdots R_i^TR_i + \cdots R_M^TR_M) + \lambda\mathbf{I}]\cdot\Delta\mathbf{x} = \Delta y_1R_1^T + \Delta y_2R_2^T + \cdots + \Delta y_iR_i^T + \cdots \Delta y_MR_M^T. \tag{A14}$$

In the case when R_i approaches 0, we have

$$\lim_{R_i\to 0}[(R_1^TR_1 + R_2^TR_2 + \cdots R_i^TR_i + \cdots R_M^TR_M) + \lambda\mathbf{I}]\cdot\Delta\mathbf{x} = \lim_{R_i\to 0}(\Delta y_1R_1^T + \Delta y_2R_2^T + \cdots + \Delta y_iR_i^T + \cdots \Delta y_MR_M^T). \tag{A15}$$

Since $\lim_{R_i\to 0} R_i^TR_i = 0$ and $\lim_{R_i\to 0}\Delta y_iR_i^T = 0$, we have

$$\lim_{R_i\to 0}[(R_1^TR_1 + R_2^TR_2 + \cdots R_{i-1}^TR_{i-1} + R_{i+1}^TR_{i+1}\cdots R_M^TR_M) + \lambda\mathbf{I}]\cdot\Delta\mathbf{x} = \lim_{R_i\to 0}(\Delta y_1R_1^T + \Delta y_2R_2^T + \cdots + \Delta y_{i-1}R_{i-1}^T + \Delta y_{i+1}R_{i+1}^T\cdots\Delta y_MR_M^T). \tag{A16}$$

Equation (A16) can be further written as

$$\lim_{R_i\to 0}\left[(R_1^T \quad R_2^T \quad \cdots \quad R_{i-1}^T \quad R_{i+1}^T \quad \cdots \quad R_M^T)\cdot\begin{pmatrix} R_1 \\ R_2 \\ \vdots \\ R_{i-1} \\ R_{i+1} \\ \vdots \\ R_M \end{pmatrix} + \lambda\mathbf{I}\right]\cdot\Delta\mathbf{x}$$

$$= \lim_{R_i\to 0}(R_1^T \quad R_2^T \quad \cdots \quad R_{i-1}^T \quad R_{i+1}^T \quad \cdots \quad R_M^T)\cdot\begin{pmatrix} \Delta y_1 \\ \Delta y_2 \\ \vdots \\ \Delta y_{i-1} \\ \Delta y_{i+1} \\ \vdots \\ \Delta y_M \end{pmatrix}. \tag{A17}$$

From Eqs. (A13) and (A17), it can be seen that the ith row R_i of the Jacobian matrix can be deleted as R_i approaches 0 during solving Eq. (8).

ACKNOWLEDGMENTS

This research is supported by Specialized Research Fund for the Doctoral Program of Higher Education (SRFDP) No. 20123201120009, Natural Science Foundation of the Jiangsu Higher Education Institutions of China No. 12KJB510029, National Natural Science Foundation of China No. 60871086, Natural Science Foundation of Jiansu Province China No. BK2008159, the Natural Science Foundation of the City of Suzhou Nos. SYG201113 and SYG201031, Hong Kong Polytechnic University (PolyU), and Australian Research Council (ARC) grants.

REFERENCES

1. Z. Xue, D. Han, and J. Tian, "Fast and robust reconstruction approach for sparse fluorescence tomography based on adaptive matching pursuit," Proc. SPIE **8311**, 831107 (2011).
2. M. Hassan and B. A. Klaunberg, "Biomedical applications of fluorescence imaging in vivo," Comput. Med. **54**, 635–644 (2004).
3. V. Ntziachristos, "Fluorescence molecular imaging," Annu. Rev. Biomed. Eng. **8**, 1–33 (2006).
4. F. Fedele, J. P. Laible, and M. J. Eppstein, "Coupled complex adjoint sensitivities for frequency-domain fluorescence tomography: theory and vectorized implementation," J. Comput. Phys. **187**, 597–619 (2003).
5. G. Zacharakis, J. Ripoll, R. Weissleder, and V. Ntziachristos, "Fluorescent protein tomography scanner for small animal imaging," IEEE Trans. Med. Imaging **24**, 878–885 (2005).
6. X. Liu, X. Guo, F. Liu, Y. Zhang, H. Zhang, G. Hu, and J. Bai, "Imaging of indocyanine green perfusion in mouse liver with fluorescence diffuse optical tomography," IEEE Trans. Biomed. Eng. **58**, 2139–2143 (2011).
7. J. Haller, D. Hyde, N. Deliolanis, R. Kleine, M. Niedre, and V. Ntziachristos, "Visualization of pulmonary inflammation using noninvasive fluorescence molecular imaging," J. Appl. Physiol. **104**, 795–802 (2008).
8. V. Ntziachristos, E. A. Schellenberger, J. Ripoll, D. Yessayan, E. Graves, A. Bogdanov, Jr., L. Josephson, and R. Weissleder,

"Visualization of antitumor treatment by means of fluorescence molecular tomography with an annexin V-Cy5.5 conjugate," Proc. Natl. Acad. Sci. USA **101**, 12294–12299 (2004).
9. A. Corlu, R. Choe, T. Durduran, M. A. Rosen, M. Schweiger, S. R. Arridge, M. D. Schnall, and A. G. Yodh, "Three-dimensional in vivo fluorescence diffuse optical tomography of breast cancer in humans," Opt. Express **15**, 6696–6716 (2007).
10. Y. Zhai and S. A. Cummer, "Fast tomographic reconstruction strategy for diffuse optical tomography," Opt. Express **17**, 5285–5297 (2009).
11. S. R. Arridge and M. Schweiger, "A general framework for iterative reconstruction algorithms in optical tomography using a finite element method," in *Computational Radiology and Imaging: Therapy and Diagnosis*, *IMA Volumes in Mathematics and Its Applications* (Springer, 1998).
12. S. G. Mallat, "A theory for multiresolution signal decomposition: the wavelet representation," IEEE Trans. Pattern Anal. **11**, 674–693 (1989).
13. F. Martelli, S. D. Bianco, and P. D. Ninni, "Perturbative forward solver software for small localized fluorophores in tissue," Biomed. Opt. Express **3**, 26–36 (2012).
14. S. R. Arridge, "Optical tomography in medical imaging," Inverse Probl. **15**, R41–R49 (1999).
15. A. P. Gibson, J. C. Hebden, and S. R. Arridge, "Recent advances in diffuse optical imaging," Phys. Med. Biol. **50**, R1–R43 (2005).
16. R. Roy, A. Godavarty, and E. M. Sevick-Muraca, "Fluorescence-enhanced optical tomography using referenced measurements of heterogeneous media," IEEE Trans. Med. Imaging **22**, 824–836 (2003).
17. M. J. Eppstein, F. Fedele, J. Laible, C. Zhang, A. Godavarty, and E. M. Sevick-Muraca, "A comparison of exact and approximate adjoint sensitivities in fluorescence tomography," IEEE Trans. Med. Imaging **22**, 1215–1223 (2003).
18. N. Ducros, "A time-domain wavelet-based approach for fluorescence diffuse optical tomography," Med. Phys. **37**, 2890–2900 (2010).
19. N. Ducros, C. D'andrea, G. Valentini, T. Rudge, S. Arridge, and A. Bassi, "Full-wavelet approach for fluorescence diffuse optical tomography with structured illumination," Opt. Lett. **35**, 3676–3678 (2010).
20. A. L. Frassati, J. M. Dinten, D. Georges, and A. D. Silva, "Model reduction using wavelet multiresolution technique applied to fluorescence diffuse optical tomography," Appl. Opt. **48**, 6878–6892 (2009).
21. L. Li and L. Qu, "Haar wavelet transform for gear fault diagnosis," Auto. Eng. **25**, 510–513 (2003).